Hybrid coupled mode modeling in 3-D: perturbed and coupled channels, and waveguide crossings

Manfred Hammer, Samer Alhaddad, Jens Förstner*
Theoretical Electrical Engineering, University of Paderborn, Germany

Abstract: The 3-D implementation of a hybrid analytical / numerical variant of coupled mode theory is discussed. Eigenmodes of the constituting dielectric channels are computed numerically. The frequency domain coupled mode models then combine these into fully vectorial approximations for the optical electromagnetic fields of the composite structure. Following a discretization of amplitude functions by 1-D finite elements, procedures from the realm of finite element numerics are applied to establish systems of linear equations for the then discrete modal amplitudes. Examples substantiate the functioning of the technique, and allow for some numerical assessment. The full 3-D simulations are highly efficient in memory consumption, moderately demanding in computational time, and, in regimes of low radiative losses, sufficiently accurate for practical design. Our results include the perturbation of guided modes by changes of refractive indices, the interaction of waves in parallel, horizontally or vertically coupled straight waveguides, and a series of crossings of potentially overlapping channels with fairly arbitrary relative position and orientation.

Keywords: integrated optics, waveguide (x-) crossings, horizontal and vertical couplers, coupled mode theory, numerical/analytical modeling.

PACS codes: 42.82.–m 42.82.Et 42.82.Gw

1 Introduction

Frequently, the functioning of a composite integrated-optical circuit can be understood in terms of the interaction of modal waves, supported by the constituting structures. Solvers for eigensolutions of these constituents (typically straight and bent dielectric channels, or optical cavities) are well established, more or less. It then remains to predict the interplay of these modes. Methods that implement this approach are typically termed "Coupled mode theory" (CMT). We refer to the articles [1, 2], to a topical collection [3], and to the textbooks [4, 5, 6, 7] for overviews on the variety of existing techniques.

CMT is often seen to motivate mere parametric models, where the coefficients in coupled mode equations serve as fit parameters, i.e. are not linked directly to the underlying basis fields / to the relevant Maxwell equations. If implemented from first principles, things are often restricted to two spatial dimensions only. There are fewer instances where non-parametric CMT formalisms have been actually applied in full 3-D. Among these are the examples of Refs. [8] (codirectional CMT, low contrast waveguides), [9, 10, 11] (codirectional CMT, higher contrast & anisotropic waveguides), [12, 13] (interaction between optical fibers and photonic crystal waveguides), or [14] (interaction between straight and bent channels, ring resonator models).

Conventionally, when working in the frequency domain (as opposed to "time domain CMT", see e.g. [15]), the wave interaction is determined as the solution of a set of ordinary differential equations, the "coupled mode equations", for the amplitudes of the basis modes, which are introduced as functions of some spatial propagation coordinate. The viewpoint of a single common propagation coordinate is decidedly unnatural, if not impracticable, for specific configurations. This concerns e.g. the coupling of waves between straight and strongly curved channels, or the crossings of waveguides, for larger crossing angles, as discussed in this paper.

A way out is found in omitting the common propagation coordinate, and, consequently, in abandoning the notion of coupled mode equations. Instead, one resorts to numerical means. The respective "Hybrid" analytical / numerical CMT variant (HCMT) has been introduced in Ref. [16], at first applied to circuits with rectangular refractive index distributions, including crossings of perpendicular waveguide channels, waveguide Bragg-gratings and related filters, or systems of coupled square microcavities [16, 17]. Refs. [18, 19] report on HCMT models of a series of micro-ring or -disk circuits. Most recent overviews of the quite versatile technique are found in Refs. [20, 21]; all examples so far, however, were restricted to 2-D.

* *University of Paderborn, FG Theoretical Electrical Engineering Warburger Str. 100, 33098 Paderborn, Germany*
Phone: ++49(0)5251/60-3560 Fax: ++49(0)5251/60-3524 E-mail: manfred.hammer@uni-paderborn.de

With this paper we report on our first results on the extension to spatially three-dimensional configurations. The modeling starts with a physically plausible expression for the electromagnetic field in the composite 3-D circuit. Suitable modes of its constituting channels (eigensolutions on 2-D cross-sectional domains) are computed numerically by means of a commercial finite-element solver [22]. Then the total field is approximated as a superposition of these vectorial profiles, with amplitudes that are functions of their — potentially different — "natural" propagation coordinates. Discretization of these into 1-D finite elements, followed by Galerkin-type projection, leads to small-size systems of linear equations. Their solutions permit to inspect the wave interaction in terms of the variations of the amplitude functions, and to assemble approximations of the overall optical fields.

The paper outlines the theoretical background, and discusses briefly limitations and implementational details. Beyond some consistency checks, our first results concern a series of quite general crossings of rectangular straight channels. Figure 1 lists the examples considered in this paper.

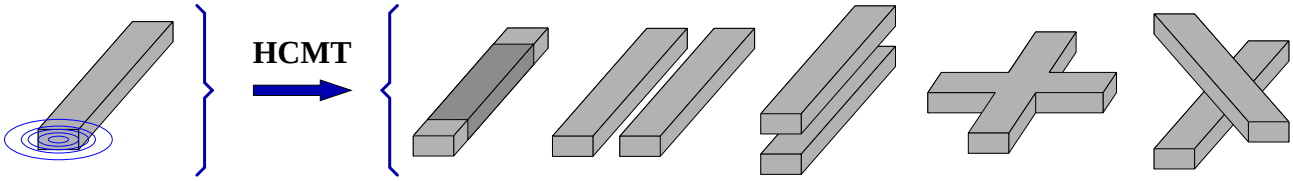

Figure 1: Hybrid coupled mode theory, schematically, here for the interaction of guided waves supported by straight dielectric channels with rectangular cross section. Given the modal properties of an isolated channel (left), the functioning of the composite systems (right) is to be predicted. Shown are a single channel with modified core permittivity, horizontally and vertically coupled parallel waveguides, a perpendicular crossing of coplanar waveguides, and intersections of channels at parallel planes with varying vertical positioning and orientation.

Our emphasis here is to show the applicability of the HCMT method for 3-D configurations, and to provide some numerical assessment. The waveguide crossings have been chosen as conveniently simple examples where conventional CMT approaches, relying on systems of coupled differential equations, are not applicable (for larger intersection angles). Still, there is interest in these structures in their own right. Simulations on waveguide crossings (2-D or 3-D, partly with optimized intersection regions, typically for waveguides on the same level) are carried out usually by numerical tools (most prominent: Finite-Difference Time Domain simulations, FDTD) [23, 24, 25, 26, 27], but also by quasi-analytical methods (2-D, mode-matching type of techniques) [28, 29]. 3-D crossings of low-contrast silica and / or polymer waveguides [30, 31, 32] have been considered as vertical couplers; switchable configurations have been simulated and realized, with small crossing angles, i.e. with nearly parallel channels, and partly designed by ("conventional") 3-D CMT [8], or by beam propagation [33]. Sections 3.4, 3.5 demonstrate the relevance of our HCMT models for the analysis of crossings in 3-D, for (nearly) the full range of intersection angles between $> 0^\circ$ up to 90°.

2 Hybrid coupled mode theory in 3-D

This concerns models in the frequency domain. A time dependence $\sim \exp(\mathrm{i}\omega t)$ is assumed for all fields, with angular frequency $\omega = k\mathrm{c} = 2\pi\mathrm{c}/\lambda$ specified by the vacuum wavenumber k or vacuum wavelength λ, for speed of light $\mathrm{c} = 1/\sqrt{\epsilon_0\mu_0}$, vacuum permittivity ϵ_0, and permeability μ_0. We seek approximate solutions of the Maxwell curl equations

$$\boldsymbol{\nabla} \times \boldsymbol{H} - \mathrm{i}\omega\epsilon_0\epsilon\boldsymbol{E} = 0, \quad -\boldsymbol{\nabla} \times \boldsymbol{E} - \mathrm{i}\omega\mu_0\boldsymbol{H} = 0. \tag{1}$$

Restricting to linear, nonmagnetic, isotropic, and lossless media, the structural properties are given by the spatially dependent refractive index n, or relative permittivity $\epsilon = n^2$, respectively.

2.1 Field template & discretization

First step towards the HCMT model is to identify a physically plausible expression for the optical electromagnetic field. Figure 2 gives a schematic representation, using the example of a waveguide channel crossing. One assumes that the total field can be approximated adequately as a superposition of the guided modes supported

by the "separated" channels. We assume here that these modal functions are at hand, being made available by suitable numerical procedures. Note that the process of "separating" the channels can be ambiguous in certain circumstances, e.g. if additional substrate or cover layers are present. To minimize errors, the supporting permittivity functions, for which the basis modes are calculated, should be as close as possible to the true, total permittivity that describes the composite structure. Depending on the phenomena that are expected (guided-wave backreflections, multimode propagation, polarization conversion), directional variants of modes of different orders and / or polarization need to be taken into account.

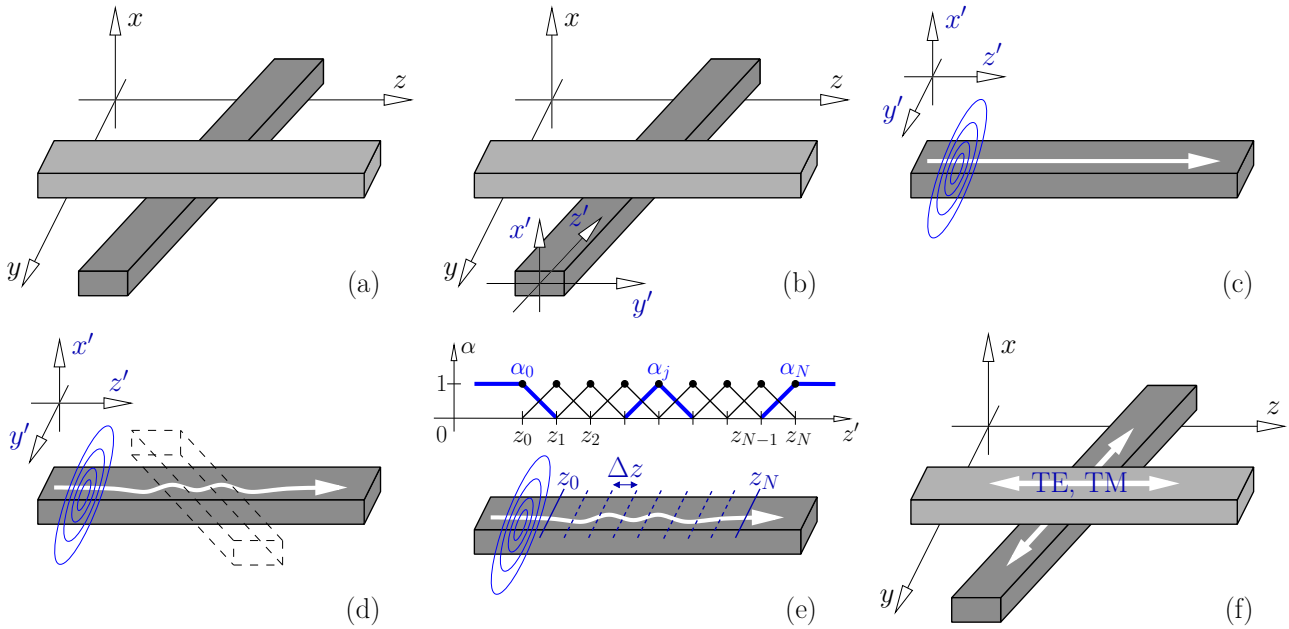

Figure 2: Hybrid numerical-analytical coupled mode model, schematically. (a) – The configuration to be analyzed, described in global Cartesian coordinates x, y, z. (b) – Convenient local coordinates x', y', z' are introduced, separately per channel and per (directional) mode. (c) – Basis fields are determined in local coordinates, including the vectorial electromagnetic mode profile, here dependent on x', y', and the exponential dependence on the "natural" propagation coordinate, here z'. (d) – An interval is identified where, due to the interaction with other elements of the composite structure, the local mode amplitude must be expected to change. (e) – Along that interaction interval, the amplitude function is being discretized by 1-D finite elements: Basis functions α_j; an equidistant discretization with $N+1$ mesh points over the interval $[z_0, z_N]$ with formally half-infinite first and last elements α_0 and α_N. (f) – Backtransformation to global coordinates and summation over respective contributions from all interacting waves leads to the final template for the total electromagnetic field.

Individually per channel, per mode, and per propagation direction, if applicable, convenient local coordinates (x', y', z') are introduced. In these coordinates, the respective mode with profile $(\tilde{\boldsymbol{E}}', \tilde{\boldsymbol{H}}')$ and propagation constant $\beta = k\, n_{\text{eff}}$, relates to the electromagnetic field [1]

$$\begin{pmatrix} \boldsymbol{E}' \\ \boldsymbol{H}' \end{pmatrix}(x', y', z') = \begin{pmatrix} \tilde{\boldsymbol{E}}' \\ \tilde{\boldsymbol{H}}' \end{pmatrix}(x', y')\, \mathrm{e}^{-\mathrm{i}\beta z'}. \tag{2}$$

One expects that the interaction with other waves changes this expression. Assuming that the original, unperturbed mode profile remains a good approximation for (part of) the field in the composite structure, an amplitude function a is introduced, that depends on the natural propagation coordinate z' of the mode. This amounts to a contribution

$$\begin{pmatrix} \boldsymbol{E}' \\ \boldsymbol{H}' \end{pmatrix}(x', y', z') = a(z') \begin{pmatrix} \tilde{\boldsymbol{E}}' \\ \tilde{\boldsymbol{H}}' \end{pmatrix}(x', y')\, \mathrm{e}^{-\mathrm{i}\beta z'}. \tag{3}$$

to the overall field, with an at present unknown function $a(z')$.

[1] In this context, the modeling of "reflected" guided waves requires two separate contributions of the form (2), one of them for the "backward" propagating mode with reversed local coordinate z'.

Here we switch to numerics. An interval is identified, outside of which a can be assumed to be constant, due to the absence of any other interacting waves. Inside the interval, a is being discretized with 1-D finite elements, i.e. a is expressed as a superposition

$$a(z') = \sum_j a_j \, \alpha_j(z') \,, \tag{4}$$

of element functions α_j, with coefficients a_j. Figure 2(e) gives an impression; for the examples in this paper we choose elements of first order on a regular mesh, with formally half-infinite first and last elements. The contribution of this particular mode then reads

$$\begin{pmatrix} \boldsymbol{E}' \\ \boldsymbol{H}' \end{pmatrix}(x', y', z') = \sum_j a_j \left(\alpha_j(z') \, \begin{pmatrix} \tilde{\boldsymbol{E}}' \\ \tilde{\boldsymbol{H}}' \end{pmatrix}(x', y') \, \mathrm{e}^{-\mathrm{i}\beta z'} \right) =: \sum_j a_j \begin{pmatrix} \boldsymbol{E}'_j \\ \boldsymbol{H}'_j \end{pmatrix}(x', y', z'), \tag{5}$$

where the last equality defines the "modal elements" $(\boldsymbol{E}'_j, \boldsymbol{H}'_j)$, products of element functions, mode profile, and modal exponential.

The backtransformation from local to global coordinates $(x', y', z') \to (x, y, z)$ concerns the position arguments as well as the orientations of the electric and magnetic field vectors. In case of the waveguide crossing, the parameters that specify the relative horizontal and vertical positioning of the waveguide cores, and the crossing angle, enter in this step. The total field is then expressed as a sum over respective contributions (5) from the different modes that are considered for the model:

$$\begin{pmatrix} \boldsymbol{E} \\ \boldsymbol{H} \end{pmatrix}(x, y, z) = \sum_k a_k \begin{pmatrix} \boldsymbol{E}_k \\ \boldsymbol{H}_k \end{pmatrix}(x, y, z). \tag{6}$$

Here all modal elements and coefficients have been merged into uniform sets, where the formal index k covers the different channels, modes of different polarization, order, and propagation direction, whatever applicable. We are left with the task to determine the coefficients a_k.

2.2 Algebraic procedure

Next we apply a projection procedure of Galerkin type, as is common in the field of finite-element numerics. The relevant Maxwell equations (1) are multiplied by trial fields $\boldsymbol{F}, \boldsymbol{G}$, and integrated. Requiring the resulting expression to vanish for arbitrary trial fields, one arrives at the weak form

$$\iiint \mathcal{K}(\boldsymbol{F}, \boldsymbol{G}; \boldsymbol{E}, \boldsymbol{H}) \, \mathrm{d}x \, \mathrm{d}y \, \mathrm{d}z = 0 \quad \text{for all } \boldsymbol{F}, \boldsymbol{G} \tag{7}$$

of Eqs. (1), with

$$\mathcal{K}(\boldsymbol{F}, \boldsymbol{G}; \boldsymbol{E}, \boldsymbol{H}) = \boldsymbol{F}^* \cdot (\boldsymbol{\nabla} \times \boldsymbol{H}) - \boldsymbol{G}^* \cdot (\boldsymbol{\nabla} \times \boldsymbol{E}) - \mathrm{i}\omega\epsilon_0\epsilon \boldsymbol{F}^* \cdot \boldsymbol{E} - \mathrm{i}\omega\mu_0 \boldsymbol{G}^* \cdot \boldsymbol{H} \,. \tag{8}$$

Inserting the field template (6), and restricting Eq. (7) to the set of modal elements $(\boldsymbol{F}, \boldsymbol{G}) \in \{(\boldsymbol{E}_k, \boldsymbol{H}_k)\}$, we are led to the linear system of equations

$$\sum_k K_{lk} a_k = 0, \quad \text{for all } l, \tag{9}$$

with overlaps of modal elements

$$K_{lk} = \iiint \mathcal{K}(\boldsymbol{E}_l, \boldsymbol{H}_l; \boldsymbol{E}_k, \boldsymbol{H}_k) \, \mathrm{d}x \, \mathrm{d}y \, \mathrm{d}z \,. \tag{10}$$

One observes that some of the coefficients a_k represent the amplitudes of incoming waves, i.e. these are given quantities. For the example of the crossing, this concerns, for every channel, mode, and propagation direction,

the coefficients of elements with index 0 (cf. the local description related to Figure 2(e)). For a model that includes bidirectional propagation of modes with both TE and TM-like polarization along both channels, these are 8 coefficients. Typically, for a single incoming polarized mode at one end of one channel, the respective single coefficient is set to one, the other 7 are zero.

The coefficients a_k are collected into a vector $\boldsymbol{a} = (\boldsymbol{u}, \boldsymbol{g})$, and ordered such that $\boldsymbol{u}$ represents the actual unknowns, while $\boldsymbol{g}$ corresponds to the given excitation. With the matrix elements (10) arranged accordingly, the system (9) can be written

$$\begin{pmatrix} \mathsf{K}_{\mathrm{uu}} & \mathsf{K}_{\mathrm{ug}} \\ \mathsf{K}_{\mathrm{gu}} & \mathsf{K}_{\mathrm{gg}} \end{pmatrix} \begin{pmatrix} \boldsymbol{u} \\ \boldsymbol{g} \end{pmatrix} = \boldsymbol{0}\,, \quad \text{or} \quad \mathsf{K}_{\mathrm{u}}\boldsymbol{u} = -\mathsf{K}_{\mathrm{g}}\boldsymbol{g}, \quad \text{with} \quad \mathsf{K}_{\mathrm{u}} = \begin{pmatrix} \mathsf{K}_{\mathrm{uu}} \\ \mathsf{K}_{\mathrm{gu}} \end{pmatrix}, \quad \mathsf{K}_{\mathrm{g}} = \begin{pmatrix} \mathsf{K}_{\mathrm{ug}} \\ \mathsf{K}_{\mathrm{gg}} \end{pmatrix}. \tag{11}$$

The matrix in the first system of Eq. (11) is square. We solve the second, overdetermined system in a least squares sense, i.e. the unknowns u are obtained as the solution of

$$\mathsf{K}_{\mathrm{u}}^{\dagger}\mathsf{K}_{\mathrm{u}}\boldsymbol{u} = -\mathsf{K}_{\mathrm{u}}^{\dagger}\mathsf{K}_{\mathrm{g}}\boldsymbol{g}\,. \tag{12}$$

Here the symbol † denotes the adjoint. Further algebraic details, and a formulation of an alternative, true variational scheme, can be found in Ref. [16].

Frequently, those coefficients $\boldsymbol{u}$ that correspond to the modal output amplitudes are already the most interesting results. After inserting the coefficients $\boldsymbol{u}, \boldsymbol{g}$, the amplitude functions (4) can give an impression of the interaction of the coupled modes. By substituting the values of $\boldsymbol{u}, \boldsymbol{g}$ for the coefficients $\boldsymbol{a}$ in Eqs. (6), one arrives at the HCMT approximation to the full field.

2.2.1 Evaluation of modal element overlaps

Given the vectorial basis mode profiles and related eigenvalues, a central part of the implementation of this scheme is the evaluation of the integrals (10). One notices that the integrand (8) requires the electric and magnetic parts of fields $\boldsymbol{E}_k$, $\boldsymbol{H}_k$ of the modal elements, but also the *curls* of these modulated modal fields. Here the following observations have been incorporated.

Keeping the direction of the local and global x, x'-directions identical, local coordinates $\boldsymbol{r}' = (x', y', z')$ and global coordinates $\boldsymbol{r} = (x, y, z)$ are related by transformations of the form $\boldsymbol{r}' = \rho(\boldsymbol{r} - \boldsymbol{r}_0)$, with a coordinate offset $\boldsymbol{r}_0$, and an orthogonal matrix

$$\rho = \begin{pmatrix} 1 & 0 & 0 \\ 0 & \cos\alpha & -\sin\alpha \\ 0 & \sin\alpha & \cos\alpha \end{pmatrix}, \tag{13}$$

which specifies a rotation by an angle α. Accordingly, fields $\boldsymbol{A}$, $\boldsymbol{A}'$ in global and local coordinates transform as

$$\boldsymbol{A}(\boldsymbol{r}) = \rho^{\mathsf{T}}\boldsymbol{A}'(\rho(\boldsymbol{r} - \boldsymbol{r}_0)). \tag{14}$$

One then readily shows that the respective curls are related as

$$(\boldsymbol{\nabla} \times \boldsymbol{A})(\boldsymbol{r}) = \rho^{\mathsf{T}}(\boldsymbol{\nabla}' \times \boldsymbol{A}')(\rho(\boldsymbol{r} - \boldsymbol{r}_0)). \tag{15}$$

In local coordinates, the basis mode fields (profiles and exponential dependence on z') satisfy the curl equations

$$\boldsymbol{\nabla}' \times \boldsymbol{H}' - \mathrm{i}\omega\epsilon_0\epsilon'\boldsymbol{E}' = 0, \quad -\boldsymbol{\nabla}' \times \boldsymbol{E}' - \mathrm{i}\omega\mu_0\boldsymbol{H}' = 0 \tag{16}$$

for the permittivity ϵ' that describes the underlying single waveguide only. ϵ' usually differs from the permittivity ϵ of the composite structure, even apart from coordinates. Further, for a field modulated as in (5),

$$\boldsymbol{A}'(x', y', z') = a(z')\bar{\boldsymbol{A}}'(x', y', z'), \tag{17}$$

one computes

$$\boldsymbol{\nabla}' \times \boldsymbol{A}' = a\boldsymbol{\nabla}' \times \bar{\boldsymbol{A}} + (\partial_{z'} a) \left(-\bar{A}'_y, \bar{A}'_x, 0)\right)^{\mathsf{T}}, \tag{18}$$

such that the local curls of the modulated basis fields are[2]

$$\boldsymbol{\nabla}' \times \boldsymbol{E}' = -\mathrm{i}\omega\mu_0 a\boldsymbol{H}' + (\partial_{z'} a) \left(-\bar{E}'_y, \bar{E}'_x, 0)\right)^{\mathsf{T}}, \quad \boldsymbol{\nabla}' \times \boldsymbol{H}' = \mathrm{i}\omega\epsilon_0\epsilon' a\boldsymbol{E}' + (\partial_{z'} a) \left(-\bar{H}'_y, \bar{H}'_x, 0)\right)^{\mathsf{T}}. \tag{19}$$

Using the recipes (15) and (19), it is possible to express the curls of the modal element fields through the exported *fields* directly, without resorting to numerical derivatives.

3 Numerical experiments

The basis mode profiles for all models in this paper have been generated by the eigenvalue solver that is part of the JCMwave software suite [22]. The computations rely on finite element methods, with unstructured, adaptive meshing, and suitable error control. Modal profiles are exported on a dense regular rectangular grid, on the transverse computational window used by the mode solver. The actual HCMT method has been implemented in C++, to some degree adapting the previous 2-D code. The programs invoke the external solver via automatically generated scripts and system calls, and import the mode profiles for further processing. In that way, any other suitable, script-driven mode solver could be supplied easily, in principle.

The evaluation of the overlaps Eq. (10) of the pairs of modal elements constitutes clearly the heaviest burden, what concerns computational time (parallelization should be straightforward, though). Accurate calculation of the integrals is required. 10-point Gaussian quadrature [34] was applied on discrete intervals of length $\leq \lambda/8$ per dimension. The procedures assume smooth integrands, hence they are deployed piecewise within regions, where the local permittivity of at least one modal element was constant; this to avoid, as far as conveniently possible, larger errors due to discontinuous field components or derivatives at dielectric interfaces. Further, the numerical integrals are evaluated piecewise on (half of the) supports of the finite element triangle functions involved. Note that each modal element (cf. Eq. (5)) comes with its own domain, given, in local coordinates, by the transverse window of the mode profile, times ($\times$) the domain of the element function $\alpha_\cdot$. Hence, for each pair of fields, the integration (10) can be restricted to the intersection of their "native" domains; the definition of a global computational domain is not necessary.

Memory requirements are mostly limited to the computation of the basis fields. These are vectorial eigenvalue problems, but on 2-D computational domains. Beyond what is required for the storage of (a pair of) the mode profiles at a time, the actual HCMT procedures require not much more memory. The final linear systems of equations to be solved are of small to moderate size, with typical dimensions of a few hundred unknowns. While no numerical discretization of 3-D field needs to be stored, after the assembly of the amplitude functions, the (approximated) fully vectorial 3-D electromagnetic field is available through the template (6).

With the present lossless contributions, the results of the HCMT models are power conservative, as far as that can be expected from a partly numerical scheme. For all simulations shown in Sections 3.2–3.5, the deviation of the relative guided power output from unity is typically well below 10^{-3}.

The examples of Sections 3.2, 3.3 permit benchmarking through direct modal analysis of the composite structure. In those cases the JCMwave eigensolver serves as reference. Assessment of the results in Sections 3.4, 3.5, however, requires "brute force" numerical calculations. Here we employed the 3-D frequency domain solver of the CST "Microwave Studio" [35], relying on a finite integration technique. Due to hardware limitations (memory), full convergence of the results, with respect to mesh step sizes and domain extension, could not always be assured. This concerns in particular some of the computationally large structures of Section 3.5 with shallow crossing angles. Still, the results should provide a suitable reference for the present purposes.

To give some indication concerning the computational effort required for a rigorous ("full Maxwell") solution, in relation to the HCMT model, we carried out reference calculations with the CST frequency-domain solver for the three crossing configurations of Figure 12, using computational parameters leading to converged results

[2] This is where the individual permittivity functions ϵ' associated with the basis fields become relevant; compare with expressions for the coupling coefficients in a conventional formulation of coupled mode theory [9].

with anticipated accuracy of ± 0.01 for the predicted transmittance levels. Table 1 compares respective runtimes and memory consumption with the computational effort for the HCMT simulations that generated the data for Figure 12. Note that the values are highly dependent on the manifold computational parameters, however the vastly reduced computational cost of the presented method is apparent in all tested scenarios.

Example:	HCMT			CST-FD		
Figure 12	memory	runtime	comp. interval	memory	runtime	comp. volume
(a), $\alpha = 70°$	150 MB	6 min	$z' \in [-1.3, 1.3]\,\mu$m	9.4 GB	1 h, 10 min	$728\,\mu$m^3
(b), $\alpha = 18.5°$	150 MB	18 min	$z' \in [-7.5, 7.5]\,\mu$m	41 GB	12 h, 48 min	$1928\,\mu$m^3
(c), $\alpha = 11°$	150 MB	28 min	$z' \in [-13, 13]\,\mu$m	92 GB	50 h, 22 min	$3157\,\mu$m^3

Table 1: Computational effort spend on simulations of the three crossing configurations of Figure 12, by the present 3-D HCMT scheme, and by the frequency-domain solver of the CST Microwave studio [35]. Observed data for peak memory use and total program runtime are compared; the extension of the computational intervals (HCMT, cf. Figure 2(e)) and the volume of the computational domain (CST) are listed. In both cases, machines with Intel 16-core Xeon CPUs (2.9 GHz) with 128 GB of memory were used. The commercial CST software (MS Windows Server) ran in parallel on up to 8 cores, depending on the phase of the computations, while our HCMT code (Linux, g++) occupied a single core only.

3.1 Basis modes

For all following simulations, we adopt parameters as given for Figure 3; these resemble values for SiO_2 / Si_3N_4 materials [36] at a typical telecommunication wavelength. For the present structures with piecewise constant permittivity, the CMT templates violate the continuity requirements of the electromagnetic fields at certain interfaces between regions with constant permittivity. The respective errors can be expected to be small, if either the contrast in refractive index itself is small, or if the local optical fields are small, where the latter condition is typically realized for high-contrast waveguides with strong light confinement. Hence, in this sense, the parameters of Figure 3, with substantial, but not too high refractive index contrast, represent a bad-case scenario for any coupled mode approach. We like to emphasize that the applicability of the HCMT approach need not be limited to "low contrast" structures. Just as for the present examples of intermediate contrast, for any "high contrast" configurations one can expect regimes of structural parameters where the HCMT models are adequate, and others, where large errors are encountered. In all cases, the specified field template (cf. Section 2.1) needs to cover the major features of the physical fields, as a prerequisite.

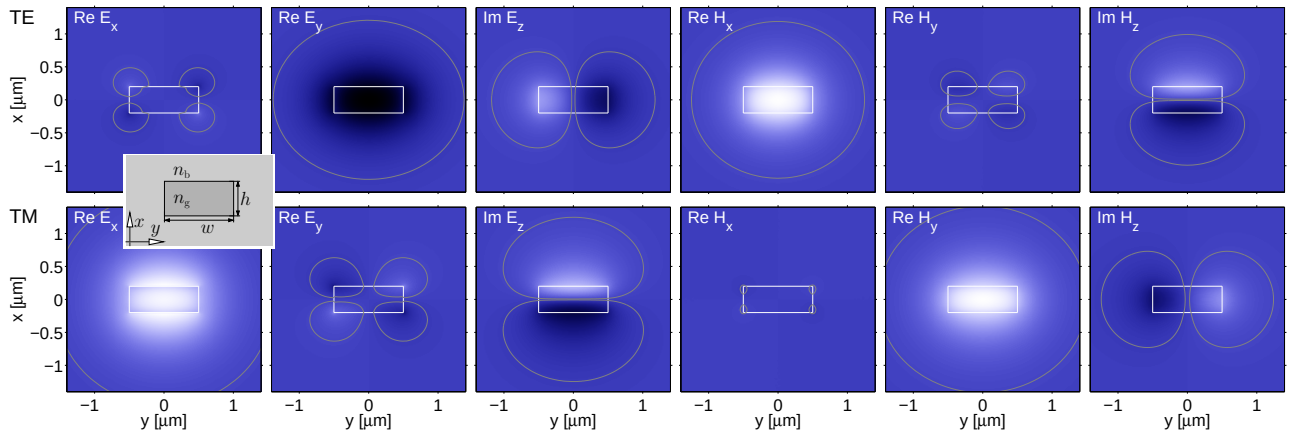

Figure 3: Electromagnetic profiles of the TE-like fundamental mode (top row), and the TM-like mode (bottom row) supported by the waveguide channels assumed for all simulations in this paper; results of the JCMwave solver [22]. Contour lines are placed at $\pm 2\%$ of the maximum levels of the absolute electric and magnetic fields strengths, determined separately for each mode. These are waveguides with a core of width $w = 1.0\,\mu$m, height $h = 0.4\,\mu$m, with core refractive index $n_g = 1.99$, surrounded by a background material with refractive index $n_b = 1.45$, at vacuum wavelength $\lambda = 1.55\,\mu$m.

The embedded rectangular strip waveguides support guided TE- and TM-like modes of lowest order only. On a computational window $(x, y) \in [-2, 2] \times [-2, 2]\,\mu$m^2, enclosed by boundary conditions of vanishing tangential electric field components ("PEC-medium"), the eigensolver [22] predicts effective indices $n_{\text{eff,TE}} = 1.63554$ and $n_{\text{eff,TM}} = 1.56809$. Note that only part of that domain is shown in the plots of Figure 3. The vectorial profiles are normalized to unit power, and exported on a dense rectangular mesh (301×301 points) for further

processing. The field extension, quantifyable by the 2%-contours shown, is slightly smaller for the fundamental TE-like mode than for the less-well confined TM mode. One thus expects, for equal geometry, a stronger interaction with other elements for the TM- than for the TE-like mode.

3.2 A single waveguide

A segment of the "native" waveguide of the basis modes serves for a first consistency check. We use a template that includes forward and backward variants of the modes of Section 3.1, with amplitudes that can vary over an interval of $10\,\mu$m length, discretized with a stepsize of $\Delta z = 0.5\,\mu$m, leading to 21 coefficients per mode, i.e. to a system (12) of dimension 80 (4 given coefficients). The forward TE mode is launched with unit initial amplitude. Figure 4(a) shows the evolution of the amplitude functions.

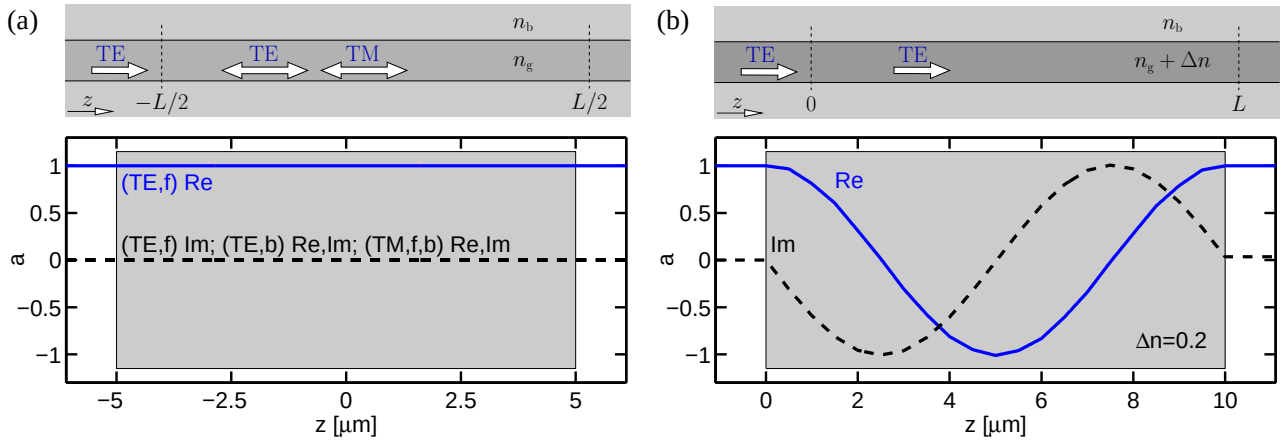

Figure 4: A single waveguide as in Figure 3, modal amplitudes a, real and imaginary parts, as function of the local propagation coordinate z. (a): the template includes forward and backward variants (f,b) of both the TE and TM modes, the TE mode is launched into its native waveguide. (b): a template that comprises the forward TE mode only, now launched into a segment with the core refractive index perturbed by $\Delta n = 0.2$.

As to be expected, the amplitude of the forward TE mode stays at $1 + 0\mathrm{i}$, while all other amplitude functions (backward TE, forward and backward TM) remain zero. The formalism predicts independent propagation of modes that are orthogonal due to different direction of propagation, or different polarization (note that these originate from an external numerical scheme).

Next we restrict the template to a single polarized forward mode at a time, but now launch that mode in a segment of the waveguide with a perturbed core refractive index (where the transitions at $z = 0, L$ are not considered). According to Figure 4(b), the amplitude no longer remains constant, but incurs a phase shift. This can be understood as follows: The perturbed waveguide supports a mode with slightly different effective index $n_{\mathrm{eff}}^{\mathrm{p}}$, i.e. with a dependence $\sim \mathrm{e}^{-\mathrm{i}kn_{\mathrm{eff}}^{\mathrm{p}}z}$ on the propagation coordinate. The HCMT scheme accommodates this through a variation of the amplitude function a, times the natural exponential dependence of the basis mode, with the original effective index n_{eff}. This amounts to a z-dependence $\sim a(z)\,\mathrm{e}^{-\mathrm{i}kn_{\mathrm{eff}}z}$. One therefore expects a variation $a(z) \sim \mathrm{e}^{-\mathrm{i}k\Delta n_{\mathrm{eff}}z}$, for an effective index perturbation $\Delta n_{\mathrm{eff}} = n_{\mathrm{eff}}^{\mathrm{p}} - n_{\mathrm{eff}}$. Table 2 compares values read off from plots as in Figure 4(b), for different polarization and levels of perturbation, with reference values, computed by direct mode analysis for the perturbed waveguide. Apparently, for fields that pass through regions with modified permittivity, the present procedures generate proper phase shifts; in this sense perturbation theory is "built into" the HCMT formalism.

Δn_{eff}	$\Delta n = 0.1$		$\Delta n = 0.2$	
	TE	TM	TE	TM
HCMT	0.075	0.049	0.154	0.100
JCMwave	0.078	0.051	0.162	0.110

Table 2: Shifts Δn_{eff}, as predicted by HCMT simulations of a waveguide segment with its core refractive index increased by Δn. Entries "JCMwave" (reference) are computed by direct mode analysis [22] of the waveguide with the perturbed core.

3.3 Parallel coupled channels

The codirectional evanescent interaction between parallel waveguides constitutes a "classical" CMT problem, in particular one where reliable benchmarking is straightforward. We consider two of the channels from Section 3.1, with the cores placed either side by side, or on top of each other, separated by some distance. Expecting neither reflections nor polarization conversion, the couplers are modeled with forward modes of the same polarization only. Figures 5, 6 summarize results for gaps of $0.2\,\mu$m. The amplitudes of the modes are discretized on an interval $z \in [0, 60]\,\mu$m with a stepsize of $0.5\,\mu$m, leading to systems (12) of dimension 240.

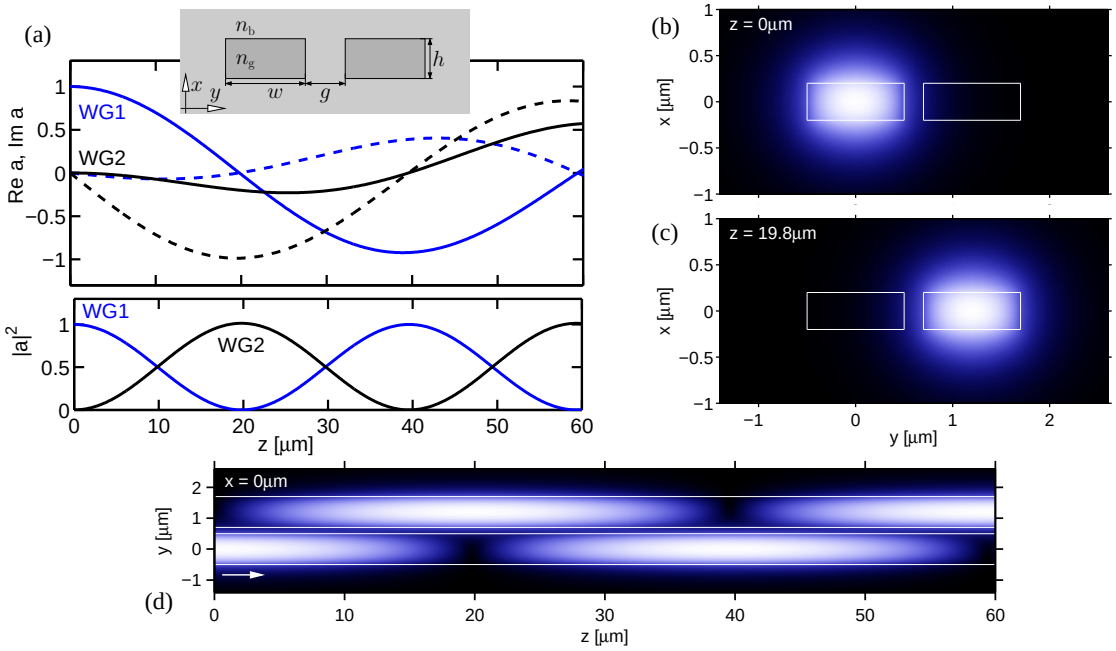

Figure 5: Horizontally coupled parallel channels. Parameters are as given for Figure 3, with the cores at a distance $g = 0.2\,\mu$m; results for TE polarized waves. (a): Amplitudes of fundamental waves associated with both waveguides cores as a function of propagation distance; real (continuous) & imaginary parts (dashed), and absolute values are shown. (b), (c): Total field (absolute value $|\boldsymbol{H}|$ of the magnetic field) at cross sections located at the input (b), and at one half-beat length (c). (d): Field $|\boldsymbol{H}|$ on the horizontal plane at the center of both cores.

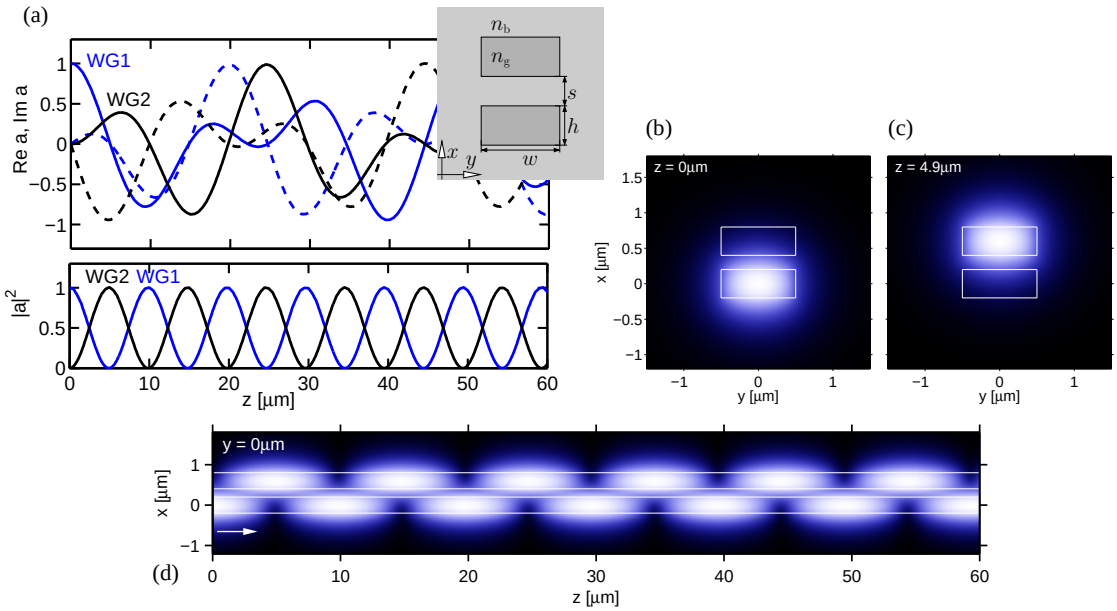

Figure 6: Vertically coupled parallel channels. Parameters are as given for Figure 3, with the cores at a distance $s = 0.2\,\mu$m; results for TE polarized waves. (a): Amplitudes of fundamental waves associated with both waveguides cores as a function of propagation distance; real (continuous) & imaginary parts (dashed), and absolute values are shown. (b), (c): Total field (absolute value $|\boldsymbol{H}|$ of the magnetic field) at cross sections located at the input (b), and at one half-beat length (c). (d): Field $|\boldsymbol{H}|$ on the vertical plane at the center of both cores.

One observes the familiar beating process, with the optical power switching periodically forth and back between the cores. Table 3 (row HCMT) lists values for the respective half beat lengths L_c, extracted from plots as in Figures 5, 6, for different gaps and polarization. As anticipated in Section 3.1, one observes a slightly stronger interaction, i.e. shorter coupling length, for the TM modes, due to the larger extent of their mode profiles. Further, for the same core separation, the interaction is much stronger for the vertically coupled setting than for horizontal coupling, due to the larger relative strengths of the basis fields at the position of the respective "other" core.

	(a) 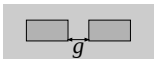						(b) 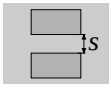							
$L_c/\,\mu$m	$g = 0.2\,\mu$m		$g = 0.3\,\mu$m		$g = 0.4\,\mu$m		$s = 0.2\,\mu$m		$s = 0.4\,\mu$m		$s = 0.6\,\mu$m		$s = 0.8\,\mu$m	
	TE	TM	TE	TM	TE	TM	TE	TM	TE	TM	TE	TM	TE	TM
HCMT	19.8	16.8	28.2	22.8	39.5	30.4	4.9	4.9	10.5	8.2	21.4	14.4	42.7	25.2
JCMwave	19.5	16.9	28.2	22.5	40.4	29.8	5.1	5.0	10.6	8.4	21.4	14.8	42.5	25.8

Table 3: Coupling lengths L_c for horizontally (a) and vertically (b) coupled waveguides with parameters as in Figure 3, as determined by the HCMT formalism, and via a direct supermode analysis with the JCMwave solver [22] (reference).

Alternatively, for the purpose of benchmarking, the two-core structure can be regarded as a single waveguide with a composite cross section, and, as such, can be analyzed directly by some mode solver. For each instance of gap and polarization, the solver returns two "supermodes" of opposite symmetry with respect to the central plane that divides the individual cores. The two propagation constants β_0, β_1 can be translated into values $L_c = \pi/|\beta_0 - \beta_1|$ for the coupling length. Table 3 shows a reasonable agreement between these reference values and the former HCMT results.

3.4 Perpendicular crossing of in-plane waveguides

As an example that is not treatable by conventional, differential-equations-based CMT, we next look at a coplanar perpendicular intersection of two of our former waveguides. Reflections and polarization conversion cannot be excluded a priori, hence the HCMT template includes bidirectional versions of TE and TM modes of both channels. The modal amplitudes are discretized on intervals $z' \in [-2.2, 2.2]\,\mu$m (local coordinates, all symmetric) with stepsize $\Delta z = 0.1\,\mu$m. For the 8 basis modes, the system (11) is of dimension 352. Figure 7 summarizes results for TE polarized excitation; we observed quite similar findings (not given) for TM excitation, with the roles of TE and TM modes reversed. Note that this is a structure with pronounced discontinuities, where scattering losses to non-guided fields are to be expected; it is thus a little daring to apply a model that is built strictly from guided fields.

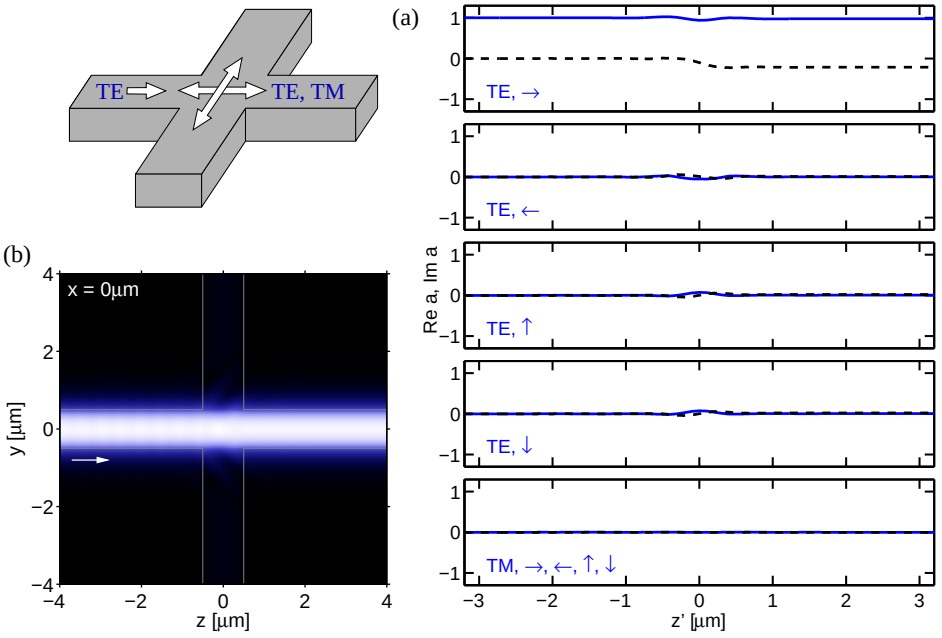

Figure 7: A perpendicular crossing of channels at the same level; parameters are as given for Figure 3. (a): Evolution of the amplitudes, real (continuous) & imaginary parts (dashed), of the directional TE and TM modes of both channels, functions of the respective local coordinates z'. Arrows indicate propagation along (→), reversed (←), or perpendicular (↑, ↓) to the direction of the incoming TE mode. (b): Total field $|\boldsymbol{H}|$ on the horizontal plane at the center of both cores.

One observes rather unexciting results. There is hardly any interaction visible; with neither reflections, redirection of power to the traversing channel, nor polarization conversion. The presence of the traversed channel becomes apparent mainly as some phase change in the propagation of the mode sent in. The modes of the lateral channel contribute slightly in the central region, without any power carried away by these fields.

Numerical reference results [35] are summarized in Table 4, that confirm the findings of small interaction between the guided modes. About 10% power loss to non-guided, radiated fields are predicted. Obviously the HCMT model cannot account for these losses. Still, as far as that is possible, given the crude approximation of negligible radiation, the HCMT simulation captures reasonably the guided part of the optical field. These findings agree well with the observations for a similar structure in 2-D [16].

(a) Input: TE				(b) Input: TM			
TE, $\rightarrow$	TE, $\leftarrow$	TE, $\uparrow,\downarrow$	TM, $\rightarrow,\leftarrow,\uparrow,\downarrow$	TM, $\rightarrow$	TM, $\leftarrow$	TM, $\uparrow,\downarrow$	TE, $\rightarrow,\leftarrow,\uparrow,\downarrow$
87%	$< 0.1\%$	$< 0.1\%$	$< 10^{-6}$	92%	$< 0.1\%$	$< 0.1\%$	$< 10^{-6}$

Table 4: For the perpendicular waveguide crossing of Section 3.4: relative guided power transferred to the polarized modal outlet straight ahead ($\rightarrow$), reflected ($\leftarrow$), and directed towards the lateral outlets ($\uparrow,\downarrow$), for TE- (a) and TM-polarized excitation (b); reference calculations using the CST solver [35].

3.5 Waveguide crossings at oblique angles

The inset of Figure 8 introduces schematically a quite general 3-D crossing of waveguides, aligned on parallel planes at different vertical levels. Given the fixed properties of the channels of Figure 3, the positioning and orientation of the cores is specified by the crossing angle α, and the vertical distance s of the horizontal center planes of the channels (here the definition of s differs from Section 3.3).

First we look at structures with fixed intersection angle, rather arbitrarily set to $\alpha = 9.44°$. Assuming negligible reflections, the HCMT model includes TE- and TM-like forward modes in the template, such that the model covers polarization conversion. The amplitudes of the 4 basis modes are discretized on computational intervals $z' \in [-15, 15]\,\mu$m (local coordinates), with stepsize $\Delta z = 0.5\,\mu$m. Figure 8 summarizes results for the transmittances along the bar light path (power remains in the excited channel) and cross light paths (power is transferred to the intersecting channel), for varying vertical positioning of the crossing waveguide and for polarized excitation. Figures 9, 10 show the evolution of the modal amplitudes and illustrate the accompanying fields, for selected vertical distances.

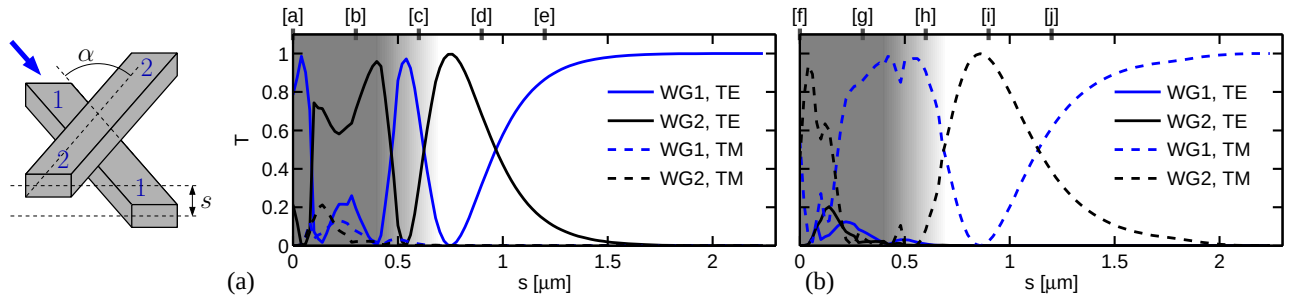

Figure 8: Intersections of two waveguides with the parameters of Figure 3, with the waveguides at parallel planes, intersecting at an angle α; polarized transmittances T as a function of the vertical center-to-center distance s between the cores, for $\alpha = 9.44°$, for the bar (WG1) and cross (WG2) paths, and for excitation by the TE-like (a) and the TM-like mode (b) in WG1. Upper labels $[a]$–$[j]$ refer to the plots of Figures 9, 10. Darker background shading indicates distances s, where the crossings potentially exhibit substantial radiative losses.

The amplitude functions displayed in Figures 9, 10 relate to superpositions of non-orthogonal basis fields. Rather, in case of small s, and at positions z' close to the center of the crossing, these are quite similar, i.e. nearly linearly dependent. There is no reason why the levels of $a_\cdot$ at intermediate positions should be restricted to $|a_\cdot|^2 \leq 1$. With power-normalized basis fields and for unit input power, the *output* amplitudes of the four basis modes satisfy the power balance $\sum |a_\cdot|^2(z_N) = 1$, with an accuracy on the scale of the figures.

While the HCMT model is thus power conservative, the physical structure must be suspected to show radiative losses. In particular for small vertical distances s with locally (partly, or entirely, at $s = 0$) merged cores, and the present shallow intersection angle, the crossing can be regarded as a combination of two Y-junctions,

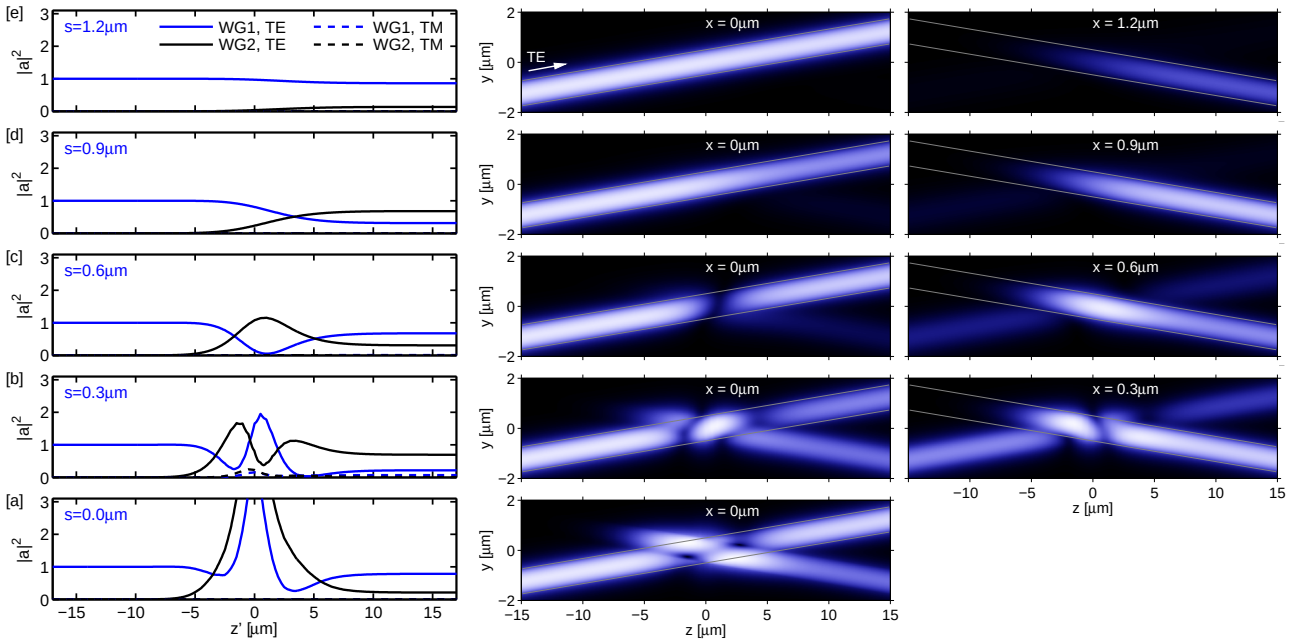

Figure 9: For the waveguide crossings of Figure 8 at angle $\alpha = 9.44°$, with TE-like excitation in WG1: Evolution of the modal amplitudes a as a function of the respective local coordinate z', and optical fields $|\boldsymbol{H}|$ at the center levels $x = 0$ of the lower and $x = s$ of the upper waveguides, for vertical distances s that correspond to the labels $[a]$–$[e]$ in Figure 8(a).

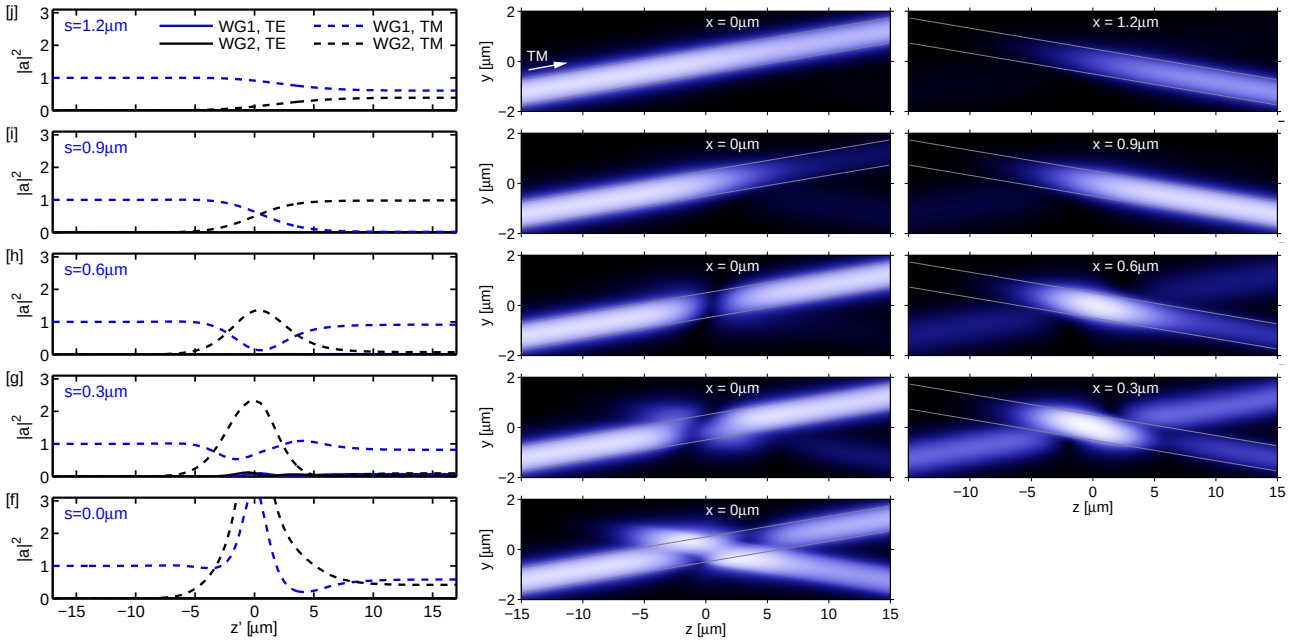

Figure 10: For the waveguide crossings of Figure 8 at angle $\alpha = 9.44°$, with TM-like excitation in WG1: Evolution of the modal amplitudes a as a function of the respective local coordinate z', and optical fields $|\boldsymbol{H}|$ at the center levels $x = 0$ of the lower and $x = s$ of the upper waveguides, for vertical distances s that correspond to the labels $[f]$–$[j]$ in Figure 8(b).

concatenated at their stems. For single-side excitation in one of the branches this might lead to about 50% power loss, as can be argued using reciprocity arguments [5]. Hence, one has to expect substantial radiation for these configurations, even without pronounced discontinuities in permittivity (as they would be present for larger intersection angles). Respective reference calculations (c.f. Figure 11) indicate that this is indeed the case. All results in Figures 8–10 for $s < 0.6\,\mu$m, say, must thus be mistrusted, in this respect. We have nevertheless included the curves, to show that the algorithm behaves reasonable, within the restrictions of the HCMT template (where one should be aware that this can be a dangerous feature).

Due to the symmetry of the setting, most reciprocity properties of the scattering matrix are trivially implemented. Beyond the geometrical symmetry, however, reciprocity demands equal transmittances for the bar and cross paths, for (orthogonal) modes of different polarizations. The matching cross-polarization curves in Figure 8(a) (dashed lines) and Figure 8(b) (continuous lines) indicate that the HCMT algorithm implements

reciprocity adequately, in this case.

Polarization conversion does apparently not play a role for larger vertical distances s, i.e. beyond the shaded region of Figure 8. Hence, for the further exploration of parameters α and s, we restrict to a template that includes unidirectional modes of one polarization only. Respective transmittance curves are shown in Figure 11. While one might argue that, for large α, e.g. for $\alpha = 90°$, the unidirectional model conflicts obviously with symmetry, the fully bidirectional simulation of Section 3.4 for the configuration $s = 0$ with the potentially strongest interaction shows that any lateral crosstalk should be negligible, at large angles, and for larger vertical separations.

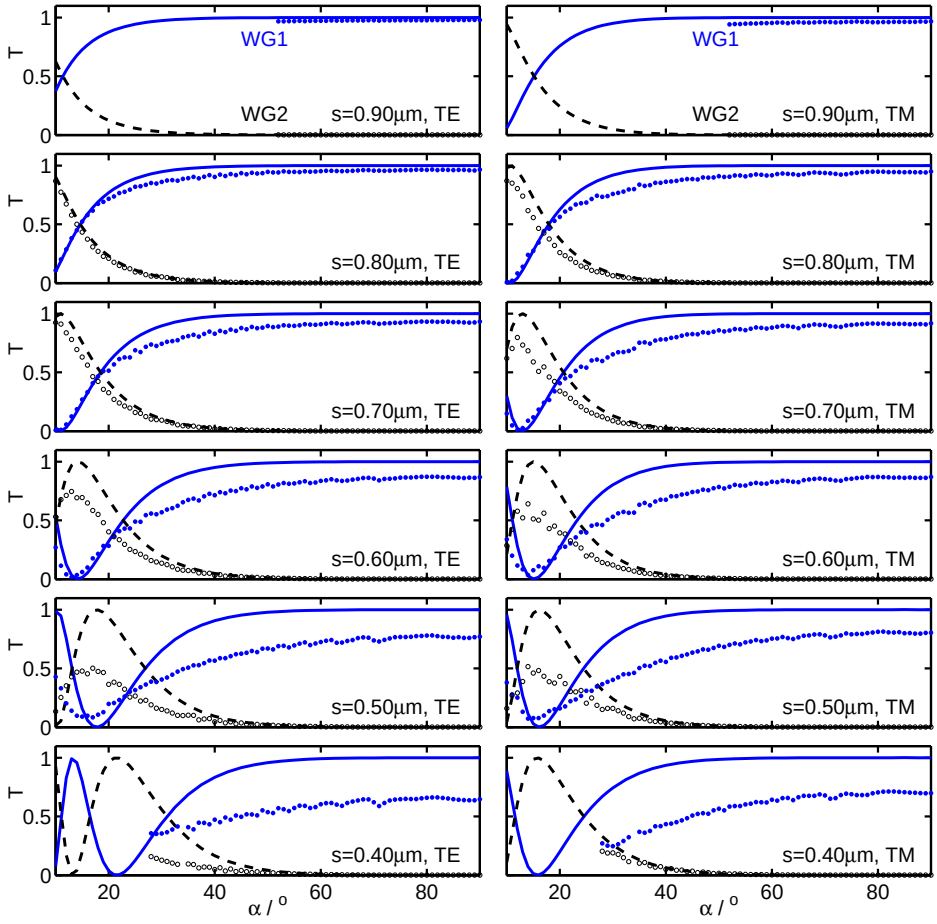

Figure 11: For oblique waveguide crossings as in Figure 8: Transmittances T as a function of the intersection angle α, for varying vertical distance s of the intersecting channels, and for TE- (left) and TM-like excitation (right). Results of a unidirectional, single polarization HCMT-model (continuous lines) and numerical reference (CST solver [35]).

Figure 11 compares the HCMT results with numerical calculations carried out with the CST solver [35]. The slightly irregular appearance those curves is caused potentially by the limited computational domain; we observed that the rippling reduces for larger distances between the waveguide cores and the transparent domain boundaries. Using those settings, however, in particular the configurations for small intersection angles were not accessible with the resources available (the required domain size depends on the intersection angle, and on the vertical distance between the waveguide cores). We therefore resorted here to the not fully converged curves.

As discussed above, the numerical reference predicts pronounced losses for smaller distances s. Still, when looking at larger separations, there is a regime with reasonable agreement between the HCMT results and the numerical reference. One observes a locally weaker interaction, but still strong net effects, with large power transfer ratios, i.e. the waveguides are obviously not decoupled at all. Here the HCMT method is most useful; with smaller radiatition losses, this is fortunately also the most interesting region for applications.

As an example, the HCMT results are reasonably close to the numerical reference for $s = 0.7\,\mu$m and TE excitation. Strong interaction can be observed, with power transfer varying from nearly zero to complete, depending on the intersection angle. Figure 12 illustrates the field characteristics for three selected crossing angles.

The findings of Figure 12 tempt to speculate on possibilities for connecting guided waves at different levels in a 3-D optical chip. Waveguide circuitry based on the present SiO_2/Si_3N_4-channels would be placed at levels with a vertical distance of $s = 0.7\,\mu$m between their center planes, operated in TE-like polarization at

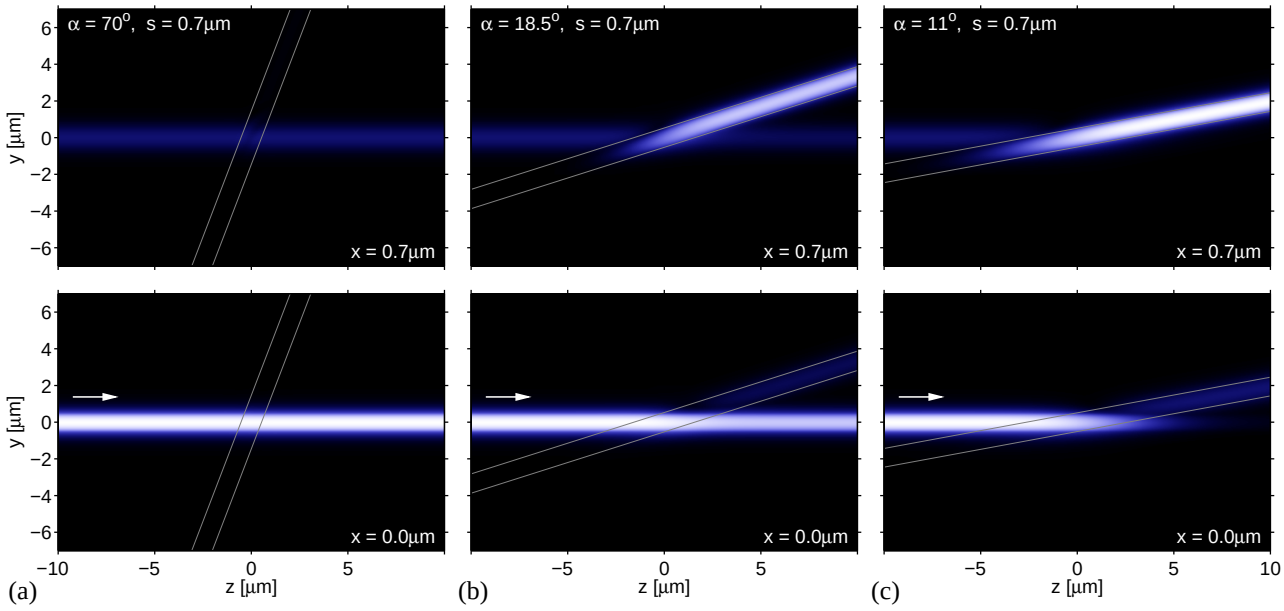

Figure 12: Optical fields $|\boldsymbol{H}|$ at the level of the lower channel $x = 0$ (bottom row) and of the upper waveguide $x = s = 0.7\,\mu$m (upper row) for crossings with intersection angles of $70°$ (a), $18.5°$ (b), and $11°$ (c). The HCMT model predicts cross-transmittances of ≈ 0 (a), of ≈ 0.5 (b), and of ≈ 1.0 (c). Parameters are as given for Figure 8.

a wavelength of $1.55\,\mu$m. Crossings of straight segments of a channel at the lower with one at the upper level could be envisioned, where the intersection angle α determines the interaction. Hardly any crosstalk to the traversing channel would be observed for nearly perpendicular crossings (angles $\geq 70°$, say). Crossings at an angle of $18.5°$ function as a 50% power splitter, those at an angle of $11°$ act as vertical couplers. All splitting ratios in between could be realized by selecting intermediate angles. Provided that the relative orientation and the vertical distance are observed, the transmittances are obviously independent from the precise relative positioning of the masks that define waveguides at the two different levels (phases depend on these positions, though).

4 Concluding remarks

The extension of the original 2-D HCMT approach [16] to fully vectorial computations for spatially 3-D configurations has been discussed. As in 2-D, efficient, quantitative, and interpretable models in the frequency domain are obtained, that are very close to common ways of reasoning in integrated optics. Up to some degree the formalism resembles a finite-element method, but one with highly specialized, structure-adapted basis functions. In the present 3-D case, the basis modes are generated numerically by an external solver. No issues related to the necessarily limited accuracy, the discrete representation, or the finite computational window of the basis modes were encountered during the implementation.

For the examples we adopted parameters with substantial, but not too high refractive index contrast, leading to potentially strong interaction of the basis fields. In case of the perturbed waveguides, and for horizontal and vertical evanescent coupling, the HCMT predictions are consistent with numerical benchmark results. For the waveguide crossings, radiation losses play a role, which the HCMT templates cannot account for. Still, where those losses are small, i.e. for the potentially most interesting configurations, we observed a good agreement with numerical reference calculations.

What concerns computational costs, the 3-D implementation is only moderately demanding in terms of both time and memory. A major part of the computational time is spent for the evaluation of modal element overlaps, where the present code leaves some room for optimization. All HCMT results shown in this paper have been generated using machines of standard desktop scale. The method thus constitutes a computationally cheap complement to much more (or, for certain cases, prohibitively) expensive rigorous numerical frequency- or time-domain calculations in 3-D.

Acknowledgments

Financial support from the German Research Foundation (Deutsche Forschungsgemeinschaft DFG, projects HA 7314/1-1, GRK 1464, and TRR 142) is gratefully acknowledged.

References

[1] S. L. Chuang. A coupled mode formulation by reciprocity and a variational principle. *Journal of Lightwave Technology*, 5(1):5–15, 1987.

[2] W. P. Huang. Coupled mode theory for optical waveguides: an overview. *Journal of the Optical Society of America A*, 11(3):963–983, 1994.

[3] D. G. Hall and B. J. Thompson, editors. *Selected Papers on Coupled-Mode Theory in Guided-Wave Optics*, volume MS 84 of *SPIE Milestone Series*. SPIE Optical Engineering Press, Bellingham, Washington USA, 1993.

[4] A. W. Snyder and J. D. Love. *Optical Waveguide Theory*. Chapman and Hall, London, New York, 1983.

[5] C. Vassallo. *Optical Waveguide Concepts*. Elsevier, Amsterdam, 1991.

[6] R. März. *Integrated Optics — Design and Modeling*. Artech House, Boston, London, 1994.

[7] K. Okamoto. *Fundamentals of Optical Waveguides*. Academic Press, SanDiego, 2000.

[8] C. M. Weinert. Three-dimensional coupled mode method for simulation of coupler and filter structures. *Journal of Lightwave Technology*, 10(9):1218–1225, 1992.

[9] M. Lohmeyer, N. Bahlmann, O. Zhuromskyy, and P. Hertel. Radiatively coupled waveguide polarization splitter simulated by wave-matching based coupled mode theory. *Optical and Quantum Electronics*, 31:877–891, 1999.

[10] M. Lohmeyer, N. Bahlmann, O. Zhuromskyy, H. Dötsch, and P. Hertel. Phase-matched rectangular magnetooptic waveguides for applications in integrated optics isolators: numerical assessment. *Optics Communications*, 158:189–200, 1998.

[11] M. Lohmeyer, N. Bahlmann, O. Zhuromskyy, H. Dötsch, and P. Hertel. Unidirectional magnetooptic polarization converters. *Journal of Lightwave Technology*, 17(12):2605–2611, 1999.

[12] P. E. Barclay, K. Srinivasan, and O. Painter. Design of photonic crystal waveguides for evanescent coupling to optical fiber tapers and integration with high-Q cavities. *Journal of the Optical Society of America B*, 20(11):2274–2284, 2003.

[13] P. E. Barclay, K. Srinivasan, M. Borselli, and O. Painter. Efficient input and output fiber coupling to a photonic crystal waveguide. *Optics Letters*, 29(7):697–699, 2004.

[14] R. Stoffer, K. R. Hiremath, M. Hammer, L. Prkna, and J. Čtyroký. Cylindrical integrated optical microresonators: Modeling by 3-D vectorial frequency domain coupled mode theory. *Optics Communications*, 256(1–3):46–67, 2005.

[15] S. Fan, P. R. Villeneuve, J. D. Joannopoulos, M. J. Khan, C. Manolatou, and H. A. Haus. Theoretical analysis of channel drop tunneling processes. *Physical Review B*, 59(24):15882–15892, 1999.

[16] M. Hammer. Hybrid analytical / numerical coupled-mode modeling of guided wave devices. *Journal of Lightwave Technology*, 25(9):2287–2298, 2007.

[17] M. Hammer. Chains of coupled square dielectric optical microcavities. *Optical and Quantum Electronics*, 40(11–12):821–835, 2009.

[18] M. Hammer. HCMT models of optical microring-resonator circuits. *Journal of the Optical Society of America B*, 27(11):2237–2246, 2010.

[19] E. F. Franchimon, K. R. Hiremath, R. Stoffer, and M. Hammer. Interaction of whispering gallery modes in integrated optical micro-ring or -disk circuits: Hybrid CMT model. *Journal of the Optical Society of America B*, 30(4):1048–1057, 2013.

[20] M. Hammer. Wave interaction in photonic integrated circuits: Hybrid analytical / numerical coupled mode modeling. In *Proceedings of SPIE*, volume 9750, pages 975018–975018–8, 2016.

[21] M. Hammer. Guided wave interaction in photonic integrated circuits — a hybrid analytical / numerical approach to coupled mode theory. In A. Agrawal, T. Benson, R. DeLaRue, and G. Wurtz, editors, *Recent Trends in Computational Photonics*, Springer Science, pages 30 pp. Springer, London, 2016, in preparation.

[22] JCMwave GmbH, Berlin, Germany; http://www.jcmwave.com.

[23] P. Sanchis, J. V. Galan, A. Griol, J. Marti, M. A. Piqueras, and J. M. Perdigues. Low-crosstalk in silicon-on-insulator waveguide crossings with optimized-angle. *IEEE Photonics Technology Letters*, 19(20):1583–1585, 2007.

[24] P. Sanchis, P. Villalba, F. Cuesta, A. Håkansson, A. Griol, J. V. Galán, A. Brimont, and J. Martí. Highly efficient crossing structure for silicon-on-insulator waveguides. *Optics Letters*, 34(18):2760–2762, 2009.

[25] W. Chang, H and Y.-H. Wu. Analysis of perpendicular crossing dielectric waveguides with various typical index contrasts and intersection profiles. In *Progress In Electromagnetics Research*, volume 108, pages 323–341, 2010.

[26] A. V. Tsarev. Efficient silicon wire waveguide crossing with negligible loss and crosstalk. *Optics Express*, 19(15):13732–13737, 2011.

[27] Y. Zhang, S. Yang, A. E. J. Lim, G. Q. Lo, C. Galland, T. Baehr-Jones, and M. Hochberg. A CMOS-compatible, low-loss, and low-crosstalk silicon waveguide crossing. *IEEE Photonics Technology Letters*, 25(5):422–425, 2013.

[28] M. Hammer. Quadridirectional eigenmode expansion scheme for 2-D modeling of wave propagation in integrated optics. *Optics Communications*, 235(4–6):285–303, 2004.

[29] R. Wang, L. Han, J. Mu, and W. Huang. Simulation of waveguide crossings and corners with complex mode-matching method. *Journal of Lightwave Technology*, 30(12):1795–1801, 2012.

[30] N. Keil, H. H. Yao, C. Zawadzki, K. Lösch, K. Satzke, W. Wischmann, J. V. Wirth, J. Schneider, J. Bauer, and M. Bauer. Hybrid polymer/silica thermo-optic vertical coupler switches. *Applied Physics B*, 73(5):469–473, 2001.

[31] K. Chen, P. L. Chu, and H. P. Chan. A vertically coupled polymer optical waveguide switch. *Optics Communications*, 244(1–6):153–158, 2005.

[32] Z. J. Cheng, Z. L. Peng, K. X. Chen, H. P. Chan, C. X. Yu, and P. L. Chu. Polymer-waveguide-based vertical coupler. *Optics Communications*, 260(2):511–513, 2006.

[33] H. J. W. M. Hoekstra. On beam propagation methods for modelling in integrated optics. *Optical and Quantum Electronics*, 29:157–171, 1997.

[34] W. H. Press, S. A. Teukolsky, W. T. Vetterling, and B. P. Flannery. *Numerical Recipes in C, 2nd ed.* Cambridge University Press, 1992.

[35] CST AG, Darmstadt, Germany; http://www.cst.com.

[36] N. Sherwood-Droz and M. Lipson. Scalable 3D dense integration of photonics on bulk silicon. *Optics Express*, 19(18):17758–17765, 2011.